Scatter And Transmission Data Fusion In An X-Ray Diffraction Imaging (XDI) Scanner

G Harding, F Isernhagen

Citation

G Harding, F Isernhagen. *Scatter And Transmission Data Fusion In An X-Ray Diffraction Imaging (XDI) Scanner*. The Internet Journal of Radiology. 2019 Volume 22 Number 1.

DOI: 10.5580/IJRA.53842

Abstract

A recently described x-ray diffraction imaging (XDI) scanner incorporates both energy-dispersive detectors for recording low-angle coherent x-ray scatter momentum profiles and dual energy x-ray transmission detectors. The x-ray scatter and transmission data originate in x-rays interacting with one and the same object. A significant improvement in the quality of information provided by the XDI scanner can be achieved when the scatter and transmission data are fused together.

Scatter and transmission data from several healthy and pathological human tissues have been analysed by a customized minimization algorithm to bring them onto a common coordinate space. This process is a prerequisite for the subsequent scatter and transmission data fusion. As indicated by results presented here, the data fusion process is computationally fast and permits the Compton and photoelectric components of the x-ray attenuation to be derived from XDI coherent scatter momentum profiles with very high accuracy. An improvement in the signal-to-noise ratio (SNR) of more than an order of magnitude results from the scatter and transmission data fusion procedure, relative to that when merely the scatter data are employed.

The sensor fusion procedure described here can be applied to all x-ray modalities, such as XDI and x-ray diffraction CT, which yield voxel specific information for the entire object space.

INTRODUCTION

A recent article published in this Journal (Harding and Isernhagen, 2018) described the potential application of an x-ray diffraction imaging (XDI) scanner to diagnostic radiology. This XDI scanner segments the 3-D object space into a complete set of contiguous voxels, each of which record the local x-ray diffraction characteristics of the corresponding object voxel. The energy-resolving scatter sensors, combined with the primary and secondary collimators, yield a 4-D data set corresponding to three spatial dimensions and one momentum dimension. The pixellated dual-energy transmission sensors, combined with the x-ray multisource, yield a
2-D data set corresponding to two spatial dimensions. A photograph of the XDI scanner for security screening applications at a major European airport is depicted in figure 1; whereas figure 2 illustrates a medical variant derived from the XDI security scanner for applications in radiology. Reference should be made to the cited publication for full details of the XDI scanner and representative results presented there.

Figure 1

Photograph of an XDI scanner for Checkpoint Baggage Screening applications (CBS) at a major European airport, courtesy of MorphoDetection GmbH Hamburg, Germany

Figure 2

Adaption of the XDI scanner depicted in Figure 1 for radiological applications. The x-ray multisource is shown at the top of the figure. The patient couch allows 2-D translational movement of the whole body through the XDI scanner fan beams. The energy-dispersive room-temperature semiconductor detectors are shown at the bottom of the figure. More details of the x-ray multisource, primary and secondary beam collimators, x-ray fan beams, scatter and transmission detectors are to be found in the article by Harding and Isernhagen (2018) and in Isernhagen (2018).

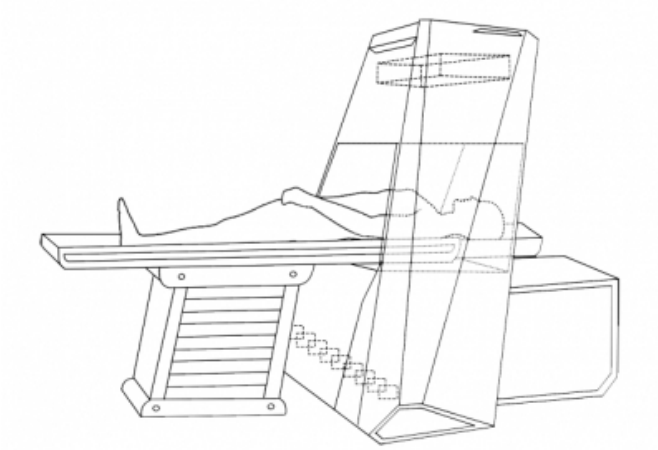

The XDI scanner features both energy-dispersive room-temperature semiconductor detectors with which the coherent scatter originating in the object is measured, as well as dual energy detectors to record the radiation transmitted through the object. The purpose of the present article is to describe the numerical process that is used to fuse together the scatter and transmission data sets, resulting in a significantly better XDI quality of information, defined as the signal-to-noise ratio (SNR), than when merely the scatter data are employed.

It is a general characteristic of electromagnetic waves propagating through non-vacuous media that their attenuation is accompanied by scattering processes originating in interactions with the attenuating medium. For the specific case of x-rays in the diagnostic energy range, taken here as running from the iodine K edge energy at 33 keV up to an upper limit set, somewhat arbitrarily, at 150 keV, there are in effect two scatter processes that contribute to the x-ray attenuation. These processes will now be described briefly.

COMPTON SCATTERING

The energy range of interest is well below the rest mass energy of the electron at 511 keV. Thus, it suffices to adopt a non-relativistic description of the Compton scattering process. Detailed descriptions of Compton scattering are to be found in standard texts such as Dyson (1990). In Compton scattering, some energy is transferred from the incoming x-ray photon to bound, atomic electrons, whereby the proportion of energy so transferred depends both on energy of the incoming x-ray and the angle of scatter as in Compton's energy shift formula (Dyson, 1990).

For non-relativistic photon energies there is an appreciable Compton back-scatter signal. Although outside the scope of this article, Compton back-scatter imaging has been used for medical, industrial (non-destructive testing) and archaeological applications (Harding, 1997).

COHERENT X-RAY SCATTER

Whereas Compton scatter is best understood as a quantum interaction, in which the incoming photon imparts energy and momentum to the scattering electron, coherent scatter is most easily understood as a classical interaction between an impinging electromagnetic wave and a spatial distribution of electrons of an atom or molecule. The incoming electromagnetic wave stimulates the electron distribution to oscillate in phase; and the resulting outgoing wave can exhibit interference effects dependent on the spatial distribution of the excited electrons.

Although the total coherent scatter cross section is small (0.09 cm-1 for 60 keV photons in water) it is highly concentrated in the forwards direction, particularly for light elements. Owing to the coherent nature of this type of scattering it exhibits interference effects related to the molecular structure of the corresponding material. The fundamental equation linking the momentum transfer, x, to the wavelength, l, of the irradiating photon is shown in equation 1, where q is the angle of scatter.

$$x = \frac{sin\,(\Theta/2)}{\lambda} \qquad (1)$$

When the wavelength is given in units of nanometres, the momentum transfer has units of reciprocal nanometres in this article.

The detector signals to the two sets (scatter and transmission) of detectors will now be briefly characterized.

SCATTER DETECTOR SIGNALS

As described in previous publications, which are referenced in Harding and Isernhagen (2018), the scatter detectors

record spatially resolved coherent scatter from the object under investigation. The scatter detectors are segmented room-temperature semiconductors (CdTe), having an energy resolution of 3 % at 60 keV. The spatial extent of the object space is 600 mm in width x 450 mm height x ¥ in the direction of the patient table movement; whereas the momentum range of the XDI scatter profiles comprises a range approximately from 0.5 nm-1 to 2.5 nm-1.

The momentum profiles of bovine femur, including both cortical and spongious components; and water, as measured with the XDI scanner are reproduced in figs 3 and 4. Referring to fig. 3, several Bragg peaks are evident. These include the 5th order collagen peak at 0.5 nm-1, which is present as collagen provides the matrix (scaffold) on which bone mineral is held. The fatty tissue peak at 1.1 nm-1 is also apparent. Finally, bone mineral (hydroxyapatite) manifests itself as the dominant peak at 1.8 nm-1 together with several other less significant peaks.

Figure 3

Momentum profile of a section of bovine femur measured with the XDI scanner. The Bragg peaks evident in the figure originate mainly from collagen, fatty tissue and hydroxyapatite (bone mineral) as described in the text.

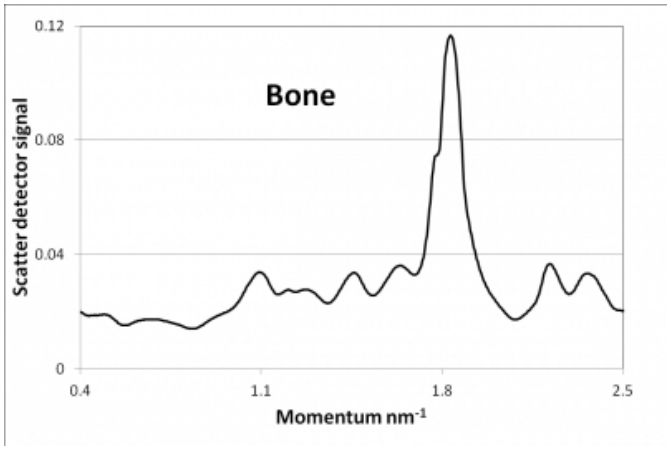

Figure 4

Momentum profile of water, an amorphous substance, as measured with the XDI scanner. In contrast to the momentum profile of bone, depicted in Figure 1, the maximum is very broad and is located at ~ 1.3 nm-1.

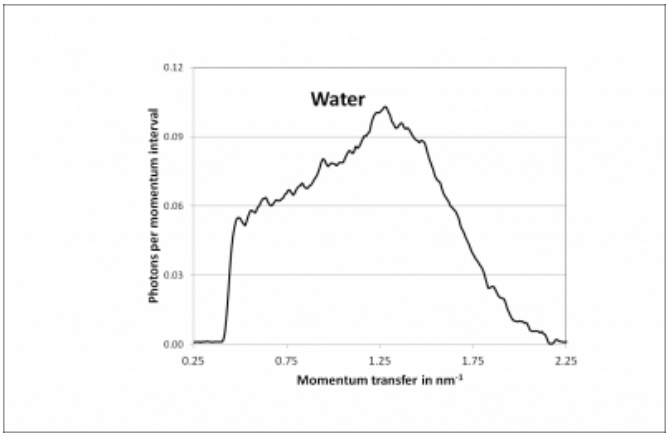

It is apparent from these results that the momentum profiles of different materials provide many features with which the materials may be classified. This classification is aided by the fact that the tissue diversity in the human body is "sparse" (Theiler et al., 2011), in the sense that human body tissues can be decomposed with the Non-Negative Matrix Factorization (NNMF) technique into a small number (primarily six) of base-tissues (Harding and Isernhagen, 2018). Additionally, the features that may be extracted from XDI momentum profiles can be transformed into linear attenuation coefficients by the technique described in section 8.

TRANSMISSION DATA SIGNALS

The transmission detectors are pixellated whereby each pixel is composed of a dual-layer of cadmium tungstate scintillators optically coupled to amorphous silicon photodiodes. The effect of the top scintillator layer is to filter the incoming x-ray beam so that its energy spectrum becomes harder before it reaches the bottom scintillator layer. Conventionally the transmission detectors are termed "dual energy" as they output two x-ray beam signals per pixel, a low energy and a high-energy signal representing the x-ray transmission at different energy levels.

The "narrow-beam" attenuation coefficient for x-rays transmitted through body tissues in the diagnostic energy range is composed in order of importance of Compton scattering, photoelectric absorption and coherent scatter, whereby the total coherent scatter is generally of negligible importance. It of course dominates the low-angle x-ray scattering as pointed out in section 2 above. Thus the linear

attenuation coefficient, μ, can be expressed as the sum of a Compton scatter term and a photoelectric term as pointed out by Alvarez and Mackovski (1976).

$$\mu(E) = A_c \cdot f_c(E) + A_p \cdot f_p(E)$$

(2)

In this equation, denotes the material-dependent Compton scatter component, having energy dependence ; whereas denotes the material-dependent photoelectric component, having energy dependence . Regarding the notation, capital " " is used in this article to denote the attenuation component along the entire ray path from x-ray source to transmission detector; whereas the lower-case " " denotes the attenuation component per voxel for x-ray modalities, such as XDI, in which voxel-dependent attenuation information is generated,

There are two alternative ways of determining the material-dependent terms and . As described by Lehmann et al., (1981), these coefficients may be derived from the high and low energy transmission detector signals by solving a second order polynomial equation. Alternatively, the coefficients may be extracted from interpolation of calibration measurements performed in the XDI scanner on an object composed of varying thicknesses of two materials, such as acrylic glass (PMMA) and aluminium. The second method was found to be more accurate and was implemented in the XDI scanner (Isernhagen, 2018). The result is that the x-ray attenuation through the object of interest is represented as a product of its transmission through equivalent thicknesses of the two materials, acrylic glass and aluminium.

It is a characteristic of the XDI scanner that it features an x-ray multisource comprising 16 independent foci as described by Harding and Isernhagen (2018). Hence each voxel in the object space is interrogated by x-rays from numerous foci to numerous transmission detectors. This characteristic allows a well-conditioned synthesis of x-ray scatter and transmission sensor data to be achieved.

The decomposition of the linear attenuation coefficient, μ(E), into two material-dependent terms as expressed mathematically in Equation 2 is illustrated for the specific case of a
15 mm thick aluminium sample in Figure 5. Two curves are presented in that figure: the red function depicts the energy-dependent transmission, T(E), defined as through the 1.5 cm thick aluminium sample, as derived from a dual-energy measurement with the XDI scanner; whereas the blue plot depicts an experimental measurement of T(E) performed with a Compton spectrometer, which will be described with explanatory references in Section 6.

The agreement in T(E) between the dual-energy and Compton spectrometer data is excellent in the energy range between 30 keV ≤ E ≤ 90 keV. Below 30 keV, there is a well known but spurious peak in the Compton spectrometer plot. This peak arises from high-energy photons that undergo multiple, predominantly second-order, Compton interactions with the detector material (germanium) of the spectrometer. The low-energy counterpart of the pair of Compton-scattered photons "mimics" a low-energy peak in the photon energy spectrum recorded by the Compton spectrometer.

Figure 5

Photon energy dependent transmission through a 15 mm thick Al sample. The red curve is derived from the "best fit" to the dual-energy decomposition expressed in equation 2; whereas the blue plot originates in measurements performed by a Compton spectrometer.

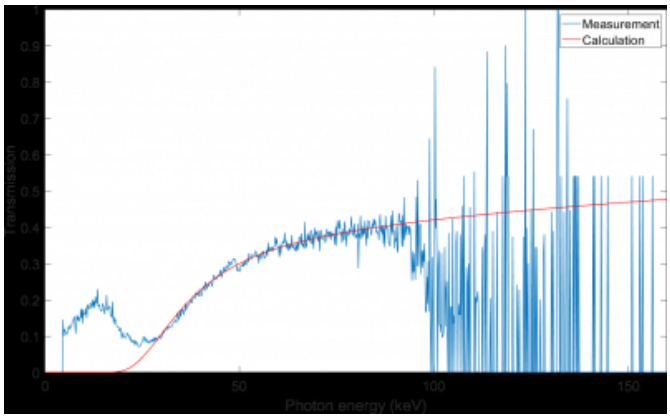

Discrepancies between the dual energy decomposition as expressed in equation 2 and the experimental Compton spectrometer plot of transmission through the aluminium sample above 90 keV are attributable to the low x-ray source radiance in the high photon energy range; and the corresponding high photon noise.

Nevertheless: there is excellent agreement as illustrated in figure 5 between the experimental Compton spectrometer plot and the dual-energy transmission curve over the energy range of interest; thus confirming the essential validity of the approach summarised here and its results.

COMPARISON OF X-RAY SCATTER AND TRANSMISSION SIGNALS

It is of interest to note that, in contrast to XDI profiles, x-ray transmission yields merely two independent parameters in

the diagnostic energy range. This is the reason why XDI momentum profiles, yielding many more features as described in the next section, outperform modalities such as computed tomography and transmission radiography in the security screening environment. It is the conviction of the present authors that the fusion of XDI scatter and x-ray transmission data, originating in one and the same object, blends the strengths of these two modalities, yielding a higher signal-to-noise ratio (SNR) for the fused data compared to the situation when either the scatter data or the transmission data are used separately to derive information concerning the object. The inherent strength of the scatter data lies in the multiplicity of features that may be extracted from XDI momentum profiles; whereas the strength of the transmission data lies in its inherently better photon statistics and thus higher statistical accuracy.

There are several ways of determining the x-ray spectrum impinging on the object under investigation. These can be broadly categorized into experimental and numerical. The most widely used experimental approach is to employ a Compton spectrometer, in which the intense x-ray beam is scattered at an angle of 90° into an energy-resolving detector (Matscheko and Ribberfors, 1987). Numerical determinations of the incoming x-ray spectrum include the semi-analytical model of Birch and Marshall (1979) and electron-photon transport programmes such as GEANT4 (Pandola et al., 2015).

The low-angle coherent x-rays are scattered at an angle of a few tens of milliradians. Thus they follow essentially the same trajectory through the object as the transmitted x-rays. Using equation 2, the transmission spectrum at all x-ray energies present in the scatter momentum profile can be determined. Hence it is possible to normalise the momentum profile against the transmission spectrum. This removes system-dependent factors, such as measurement time, scan rate and x-ray source power from the scatter momentum profiles. The theoretical basis for the normalization of low-angle coherent scatter against the transmitted spectrum has been given by King and Johns (2010).

XDI MOMENTUM PROFILE FEATURES

The task at hand before data fusion may be achieved is to find a relationship between XDI momentum profiles, as measured with the scatter detectors of the XDI scanner, and the Compton and photoelectric components of the attenuation coefficient, as measured with the transmission detectors of the XDI scanner.

X-ray diffraction (XRD) is a gold standard for identification of powder crystalline materials; and there are numerous compilations such as that of the International Centre for Diffraction Data (ICDD) permitting material characterization of organic and inorganic samples, for example that of the bovine femur pattern depicted in figure 1, on the basis of the locations and intensities of the Bragg peaks that they produce. It may be surprising that the diffraction profiles of amorphous materials such as that of water depicted in figure 4 also yield a multiplicity of features enabling characterization and classification. It has been known for some time (Harding et al., 2010) that x-ray diffraction profiles of non-crystalline substances not only permit liquid, amorphous and gels (LAGs) to be classified, but also allow their transformation into the Compton and photoelectric components of the linear attenuation coefficient. For the sake of simplicity, these non-crystalline materials will be referred to below simply as amorphous.

A complete list of the XDI features permitting characterization and classification of amorphous substances has been given elsewhere (Harding et al., 2010; Isernhagen, 2018). In all cases the XDI momentum profile is normalized such that system and object-dependent factors such as x-ray tube power, measurement time and object transmission are accounted for. An important insight into XDI of amorphous substances is that, whereas the positions of individual molecules are constantly changing over time owing to diffusion, the substances are characterized by a corresponding mean intermolecular separation that manifests itself in a principal peak whose position and shape can be exploited to characterize the substance.

The main features, of which only a few of the more important ones are described here, are as follows. The scatter strength, S, is defined as the total voxel-dependent normalized XDI scatter signal summed over the momentum range from 0.5 to 2.25 nm-1. The normalized XDI signal in the low momentum range summed from 0.5 to 0.75 nm-1 is termed C, as it is related to the isothermal compressibility of the material in the voxel. The principal peak position, P, which has the value for water of 1.6 nm-1 is related to the statistically averaged inverse mean intermolecular distance. The gradient, G, of the high momentum decay to zero between 1.75 nm-1 and 2.25 nm-1 is related to the mean atomic number of material in the voxel.

MINIMIZATION PROCEDURE

Denoting the features of the XDI profiles summarized in the

previous section, as F[1], F[2], ... F[N], the task at hand is to determine the values of the weights [1], [2], ..., [N], together with the coefficients [1], [2], ..., [N], with which the Compton and photoelectric components of the attenuation respectively may be calculated from XDI profiles. In mathematical form, when these coefficients have been determined, the voxelized Compton component of the attenuation is represented by , which is extracted as a product of the weights multiplied by the numerical values of the XDI features. This relationship is expressed in equation 3.

$$a_c = \sum_{I=1}^{N} w_c[I] \cdot F[I] \qquad (3)$$

There is a completely analogous equation for ; representing the weights with which the XDI profile features allow the photoelectric component of the voxelized attenuation to be determined. The optimization procedure can be performed in several alternative ways. Intuitively, the simplest is a "brute-force" method in which all combinations of features and weights are computed until that combination is found that leads to the most accurate fit between the measured values of and and those derived from XDI profile features, in a least squares deviation sense. Alternatively, equation 3 can be solved by an iterative "Simplex" procedure as described e.g. by Schriver, (1998). This method was chosen because of its speed and accuracy. Further details are to be found in Isernhagen (2018). For the 12 "in vitro" biomedical tissues listed in Harding and Isernhagen (2018) the linear attenuation coefficient could be reproduced with the aid of equation 3 to an excellent overall accuracy of 0.5 % standard deviation at 60 keV.

It is extremely important that the weighting coefficients be accurately determined. For this purpose the XDI scanner is operated in "reference" mode allowing an arbitrarily long scan time per object cross-section. The ensuing scatter data may then be regarded as noise- and systematic error-free. Knowledge of the and components of the linear attenuation from equation 3, together with the obliquity of the impinging x-ray beam, permits the integrated attenuation along an x-ray beam propagating from an x-ray multisource focus to a scatter detector pixel to be determined. This in turn provides a direct comparison with the and values as determined for the same beam by a transmission detector pixel. If the two sets of data are found to be inconsistent, the numerical values of the features, but not the weights in equation 3, are "nudged" to bring the scatter data more into line with the transmission data. That it is why it is so important to have accurate values of the weights in equation 3. This procedure is repeated iteratively and after each iteration the features are updated.

The and values derived from the x-ray scatter sensors with the aid of equation 3 are summed over the corresponding beam path from focus to transmission detector to yield scatter and values. The and values measured by the transmission sensors are compared to those of the scatter data, yielding the two differences and . These are back-projected along the corresponding beam path; and the differences are assigned to individual voxels along the path in proportion to their local and intensities. Naturally, if there were only one ray path per voxel, this process would merely maintain the relative intensities of the and values from the previous iteration.

The XDI scanner features an x-ray multisource comprising 16 foci. There are 17 transmission detectors. Thus the object space is sampled with 272 independent x-ray beams. Each object voxel is traversed on average by four x-ray beams. Owing to statistical noise, each voxel will sometimes exhibit a higher scatter intensity and sometimes a lower intensity than its mean value. For the sake of simplicity it is assumed that the scatter intensity distribution per voxel is symmetric. The probability that the four independent measurements of voxel scatter intensity compensate one another to a certain extent is over 90 % (1-2-4).

As the features are extracted from the entire momentum range of the XDI profile, essentially an updated momentum profile ensues. This procedure is repeated iteratively until some termination criterion has been achieved. The intention underlying this procedure is to determine that object that best matches the x-ray scatter and transmission data.

RESULTS OF X-RAY SCATTER AND TRANSMISSION DATA FUSION

To give an impression of the results of x-ray scatter and transmission data fusion, attention is drawn to figure 6, showing two polyethylene bottles that were later filled with water and analysed in the XDI scanner. The larger of the two bottles had dimensions of 60 mm diameter and 125 mm overall height, leading to an enclosed volume of 250 ml. The cap of the bottle is nominally 17 mm high. To ensure closure of the bottle contents, the neck has a flared region of 1 mm thickness against which the cap mates as it is screwed

down.

Figure 6

Polyethylene (PE) bottles of 125 and 250 ml volume that were used as test objects in the XDI scanner to test the efficacy of scatter and transmission data fusion.

When merely the scatter strength without transmission data fusion is used to characterize the water contents of these bottles, the mean standard deviation as measured over all voxels in the bottles is 0.36 on a scale for which the scatter strength for water is unity. This high noise result is illustrated for the 250 ml bottle in Figure 6. On combining scatter and transmission data, the standard deviation is reduced by more than an order of magnitude to 0.022 as displayed in figure 7.

Figure 7

Scatter strength image of the 250 ml water bottle when merely the scatter data are employed.

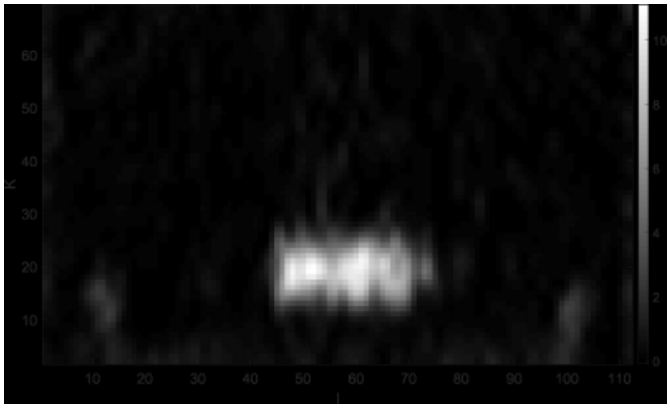

The cross-sectional dimensions of the bottle are indicated by the white lines superimposed on the scatter strength image of figure 7. This figure gives an impression of the spatial resolution of the XDI scanner. Referring to figure 5 and figure 7, the joint of cap and neck is possibly indicated in figure 7 as a region of enhanced scatter strength in the neck region. The parameter depicted is once again the scatter strength as defined above.

Figure 8

Enlarged scatter strength cross-sectional image of water bottle depicted in Figure 5. The physical dimensions of the bottle, measured to be 60 mm diameter and 125 mm overall length are represented as the white lines superimposed on the scatter strength gray scale image, to give an impression of the XDI scanner spatial resolution.

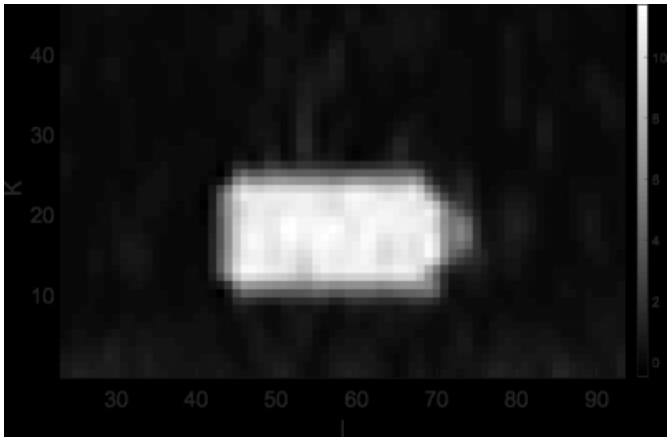

CONCLUSIONS

It is noteworthy that, as demonstrated in section 8, the linear attenuation coefficients of biomedical tissues can be determined with high accuracy from their XDI momentum profiles. Together with the dual-energy transmission data provided by the XDI scanner, it is possible to bring both the

XDI scatter and transmission data onto a common coordinate space. Combination of the scatter and transmission data in the XDI scanner permits an improvement in the signal-to-noise ratio of water bottles of varying positions, orientations and volumes having unit scatter strength of more than an order of magnitude, in which the relative noise of the scatter strength is reduced by more than an order of magnitude from 36 % to 2.2 %.

These numerical results are illustrated in figure 6 and figure 7 by measurements of scatter strength performed on a 250 ml water bottle. Whereas figure 6 merely employs the scatter data from the XDI scanner, figure 7 fuses both scatter and transmission data to achieve a remarkable improvement in the signal-to-noise ratio (SNR). Based on these numerical results and images it is the strong conviction of the authors that in situations where high scan speeds are necessary, such as in diagnostic radiology, fusion of the x-ray scatter and transmission sensor data can lead to a remarkable improvement in the scatter strength signal-to-noise ratio.

The fusion procedure described here can be implemented on all x-ray modalities, such as XDI and x-ray diffraction CT, which give voxelized information for all voxels in the object space.

Acknowledgement

It is a pleasure to acknowledge the many fruitful discussions with Dr J. P. Schlomka, erstwhile leader of the engineering group at MorphoDetection, Hamburg.

References

1. Alvarez R E and Macovski A. (1976) Energy-selective reconstructions in X-ray computerized tomography Phys Med Biol., 21, 733 – 744.
2. Birch R and Marshall M (1979) Computation of bremsstrahlung X-ray spectra and comparison with spectra measured with a Ge(Li) detector Phys. Med. Biol. 24, 505 – 517.
3. Dyson N A (1990) X-rays in atomic and nuclear physics (2nd edition Cambridge University Press: Cambridge)
4. Harding G (1997) Inelastic photon scattering: Effects and applications in biomedical science and industry Rad. Phys. Chem. 50, 91 – 111.
5. Harding G and Isernhagen F, (2018) A potential application of an X-Ray Diffraction Imaging (XDI) scanner in diagnostic radiology, Int. Jour. Radiol., 21, 1 – 10.
6. Harding G, Fleckenstein H, Olesinski S, Zienert G, (2010) Liquid detection trial with x-ray diffraction, Proc. SPIE 7806, Penetrating Radiation Systems and Applications XI, 78060G.
7. Isernhagen C F, (2018) Röntgendiffraktionsbildgebung: Von der Röntgenbeugung zur optimierten Bildrekonstruktion, (Infinite Science Publishing: Lübeck, Germany)
8. Lehmann L A, Alvarez R E, Macovski A, Brody W R, Pelc N J, Riederer W J and Hall A L, (1981) Generalized Image Combinations in Dual KVP Digital Radiography, Medical Physics, 8, 659 – 667.
9. King B W and Johns P C, (2010) An energy-dispersive technique to measure x-ray coherent scattering form factors of amorphous materials Phys. Med. Biol. 55 855–871.
10. Matscheko G and R Ribberfors R (1987) A Compton scattering spectrometer for determining X-ray photon energy spectra Phys. Med. Biol. 32 577 – 594.
11. Theiler J, Cao G, Bachego L R and Bouman C A, (2011) Sparse Matrix Transform for Hyperspectral Image Processing, IEEE Jour. Select. Topics in Signal Processing, 5, 424 – 437.
12. Pandola L, Andenna C, Cacccia B, (2015) Validation of the GEANT4 simulation of bremsstrahlung from thick targets below 3 MeV Nucl. Instr. Meth. B, 350, 41 – 48.
13. Schrijver A, (1998) Theory of Linear and Integer Programming, (Wiley: New York).

Author Information

Geoffrey Harding
Adelphis Commercial Enterprises

Fabian Isernhagen
Adelphis Commercial Enterprises